

See discussions, stats, and author profiles for this publication at: <https://www.researchgate.net/publication/46217826>

Double-quantum two-dimensional electronic spectroscopy of a three-level system: Experiments and simulations

ARTICLE in THE JOURNAL OF CHEMICAL PHYSICS · SEPTEMBER 2010

Impact Factor: 2.95 · DOI: 10.1063/1.3474995 · Source: PubMed

CITATIONS

26

READS

54

8 AUTHORS, INCLUDING:



Alexandra Nemeth

University of Vienna

15 PUBLICATIONS 365 CITATIONS

SEE PROFILE



Tomas Mancal

Charles University in Prague

66 PUBLICATIONS 2,784 CITATIONS

SEE PROFILE



Tõnu Pullerits

Lund University

180 PUBLICATIONS 5,466 CITATIONS

SEE PROFILE



Jaroslav Sperling

University of Vienna

35 PUBLICATIONS 675 CITATIONS

SEE PROFILE

Double-quantum two-dimensional electronic spectroscopy of a three-level system: Experiments and simulations

Alexandra Nemeth,^{1,a)} Franz Milota,¹ Tomáš Mančal,² Tõnu Pullerits,³ Jaroslav Sperling,⁴ Jürgen Hauer,¹ Harald F. Kauffmann,^{1,5} and Niklas Christensson^{1,3,b)}

¹*Electronic Properties of Materials, Faculty of Physics, University of Vienna, Strudlhofgasse 4, Vienna 1090, Austria*

²*Institute of Physics, Faculty of Mathematics and Physics, Charles University, Ke Karlovu 5, Prague 121 16, Czech Republic*

³*Department of Chemical Physics, Lund University, Box 124, SE-21000 Lund, Sweden*

⁴*Newport Spectra-Physics, Guerickeweg 7, Darmstadt 64291, Germany*

⁵*Ultrafast Dynamics Group, Faculty of Physics, Vienna University of Technology, Wiedner Hauptstrasse 8-10, Vienna 1040, Austria*

(Received 26 April 2010; accepted 14 July 2010; published online 2 September 2010)

Double-quantum coherence two-dimensional (2Q2D) electronic spectroscopy is utilized to probe the dynamic fluctuations of electronic states in a solvated molecule at approximately twice the energy of the ground state bleach transition. The 2Q2D spectrum gives insight into the energetic position and spectral fluctuations (system-bath interaction) of the probed excited states. Combining it with single-quantum two-dimensional (1Q2D) electronic spectroscopy enables one to determine the strength of the excited state absorption transition and the relative detuning of electronic states, as well as the dynamics of the single-quantum coherence. To investigate the correlation of spectral fluctuations in different electronically excited states, we have carried out experiments on a solvated dye (Rhodamine 6G) with 23 fs pulses centered at the maximum of the linear absorption spectrum. The 2Q2D spectrum reveals three peaks of alternating signs with the major negative peak located at higher frequencies along the emission axis compared to the single positive peak. The 1Q2D spectrum, on the other hand, shows a negative peak stemming from excited state absorption at lower frequencies along the emission axis. Analysis of the signal in the homogeneous limit fails to account for this observation as well as the number of peaks in the 2Q2D spectrum. Employing a three-level model in which all time correlations of the third-order response function are accounted for via second-order cumulant expansion gives good agreement with both the 1Q2D and 2Q2D data. Furthermore, the analysis shows that the fluctuations of the probed electronic states are highly correlated, reflecting the modulation by a common nuclear bath and similarities in the nature of the electronic transitions. © 2010 American Institute of Physics. [doi:10.1063/1.3474995]

I. INTRODUCTION

During the past decade, coherent multidimensional spectroscopy has become an important method for studying condensed phase electronic and nuclear dynamics with femtosecond time resolution.^{1–3} Being derived phenomenologically from multidimensional NMR spectroscopies, two-dimensional electronic spectroscopy (2D-ES)^{4,5} investigates electronic and nuclear dynamics by correlating the time evolution of electronic and vibronic coherences during two time intervals. Unlike in NMR, optical experiments are subject to the phase matching condition, and spatial filtering allows one to isolate specific polarization components induced in the sample.

Typically, 2D-ES experiments are carried out in third order with respect to the electric field and in a noncollinear geometry.⁴ After three interactions with pulsed electromagnetic fields, the sample radiates a third-order nonlinear signal

field in the phase matching directions $\mathbf{k}_I = -\mathbf{k}_1 + \mathbf{k}_2 + \mathbf{k}_3$ [S_I , rephasing single-quantum two-dimensional (1Q2D)], $\mathbf{k}_{II} = +\mathbf{k}_1 - \mathbf{k}_2 + \mathbf{k}_3$ (S_{II} , nonrephasing 1Q2D), and $\mathbf{k}_{III} = +\mathbf{k}_1 + \mathbf{k}_2 - \mathbf{k}_3$ [S_{III} , double-quantum coherence two-dimensional (2Q2D)].⁶ The different experimental techniques, their corresponding Feynman diagrams, and a representative signal calculated for a three-level system in the homogeneous limit are shown in Fig. 1. In this contribution, we will focus on ladder-type three-level systems consisting of a ground state $|g\rangle$, a first excited state $|e\rangle$, and a second excited state $|f\rangle$. Signals along \mathbf{k}_I and \mathbf{k}_{II} arise already for electronic two-level systems and involve only single-quantum coherences (e.g., $|e\rangle\langle g|$).^{6,7} S_I and S_{II} techniques (and most of all, their sum, $S_I + S_{II}$) have been used extensively to study electronic and nuclear dynamics in the visible and infrared spectral regions.^{2,3}

In contrast to S_I and S_{II} experiments, the signal along \mathbf{k}_{III} can only be observed for systems with at least three electronic levels, thus being predestined for probing electron correlation effects.⁸ This is due to the particular ordering of the fields, i.e., the first two pulses interact with the same

^{a)}Author to whom correspondence should be addressed. Electronic mail: alexandra.nemeth@univie.ac.at.

^{b)}Electronic mail: niklas.christensson@univie.ac.at.

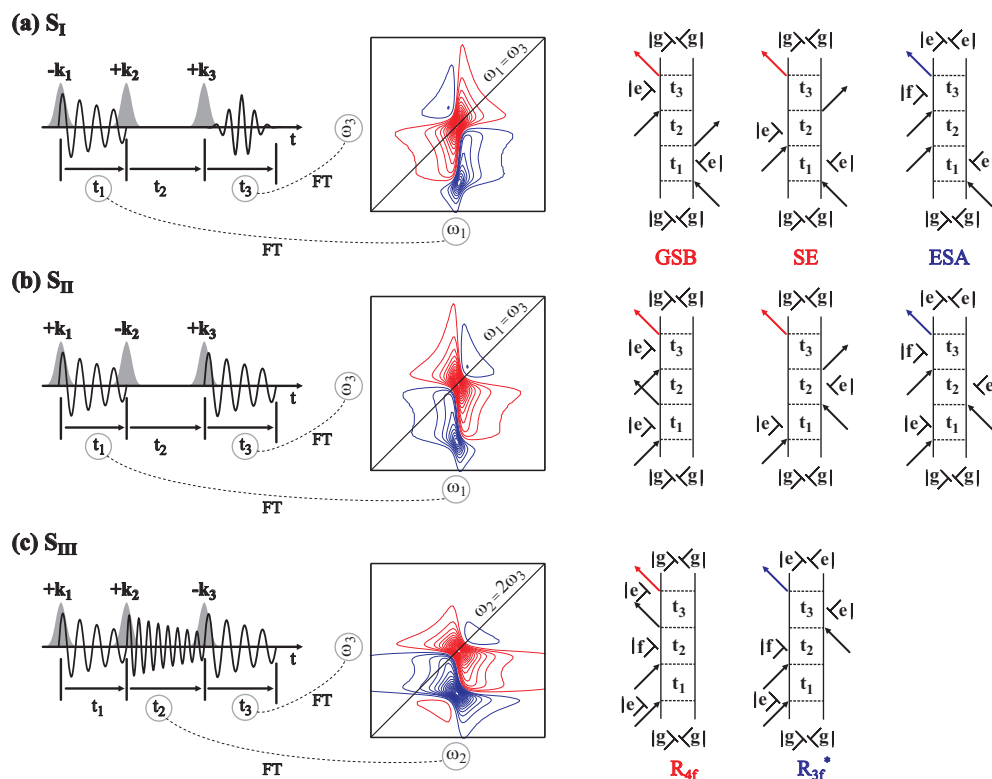


FIG. 1. Schematic of the three two-dimensional methods S_I (a), S_{II} (b), and S_{III} (c). An illustration of the coherence evolution and the Fourier transform used to construct the correlation spectra is shown in the leftmost column. Both S_I and S_{II} correlate the single-quantum coherence evolution of the system during t_1 and t_3 for a fixed waiting time t_2 . For S_{III} , all three propagation periods involve coherences and the double-quantum coherence propagation during t_2 leads to oscillations at roughly twice the frequency of the single-quantum coherence. The 2Q2D spectrum is constructed by correlating the double-quantum coherence evolution during t_2 with the single-quantum coherence evolution during t_3 . In the central column, we show model calculations of the real part of the S_I , S_{II} , and S_{III} signals based on the homogeneous limit of a three-level system with equal transition dipole moments and a redshifted second excited state. This model is more extensively discussed in Sec. IV A. The rephasing (S_I) [nonrephasing (S_{II})] 1Q2D signal exhibits its characteristic orientation parallel (perpendicular) to the diagonal line. The 2Q2D signal (S_{III}) shows strong similarities with the nonrephasing 1Q2D signal (S_{II}). The Feynman diagrams contributing to each signal are depicted in the rightmost column. Here, $|g\rangle$, $|e\rangle$, and $|f\rangle$ denote the ground, first excited, and second excited states, respectively. Red (blue) signal arrows indicate positive (negative) signal contributions.

sign, thereby inducing a double-quantum coherence $|f\rangle\langle g|$ that oscillates during t_2 with approximately twice the frequency of a single-quantum coherence ($\omega_{fg} \approx 2\omega_{eg}$). The interaction of the third pulse determines the sign of the contribution, which is positive in case the third pulse acts on the *bra*-side, creating a $|e\rangle\langle g|$ -coherence, or negative in case it acts on the *ket*-side and creates a $|f\rangle\langle e|$ -coherence.⁹ Consequently, while for S_I and S_{II} Fourier transform along t_1 and t_3 correlates two single-quantum coherences oscillating at $\approx \omega_{eg}$, S_{III} correlates the double-quantum coherence evolution at ω_{fg} during t_2 with a single-quantum coherence oscillating at $\approx \omega_{eg}$ during t_3 (Fig. 1).

The three-level system required for the observation of the 2Q2D signal arises naturally in the spectroscopy of vibrational modes in the IR spectral region, where 2Q2D spectroscopy has been employed to measure diagonal and off-diagonal anharmonicities.¹⁰ For electronic transitions, one should expect that higher lying electronic states are accessible within the bandwidth of the excitation pulses (i.e., with an energy of $\approx 2\omega_{eg}$ with respect to the ground state). In mean field models of electronic structure, such as Hartree–Fock, there is a state at twice the HOMO–LUMO (highest occupied molecular orbital–lowest unoccupied molecular orbital) energy with a wave function that is given by a double HOMO–LUMO excitation.^{8,11} We will refer to this type of

state as a doubly excited state in this contribution. Neglecting the coupling to a nuclear bath (see Sec. IV B), the mean field model predicts that the signal vanishes due to destructive interference of the Feynman pathways contributing to the signal (cf. Fig. 1).⁸ Going beyond mean field models, electron correlation and exchange effects will shift the electronic states, thereby lifting the cancellation of the signal.^{8,12,13} In systems where electron correlation and exchange effects are small, such as semiconductors or molecular aggregates, the shift of the second excited state relative to the first gives information about the biexciton binding energy, i.e., the binding energy of the two-electron-hole pair quasiparticle. The binding energy and the dynamics of the nonradiative two-exciton states have been investigated in GaAs quantum wells.^{14,15}

Recently, 2Q2D electronic spectroscopy has been applied to molecules in solution.^{16,17} In contrast to semiconductors,¹⁸ quantum wells,^{12,14,15,19} and molecular aggregates,⁹ molecules often display large electron correlation and exchange effects (of the order of eV).^{20,21} The changes of the energy levels due to these effects can thus easily shift the doubly excited state out of the bandwidth of the laser pulses used in the experiments.¹³ However, in molecules, there is usually a large number of electronically excited states in the vicinity of $2\omega_{eg}$ and some of these states

may give rise to a S_{III} signal. Due to the strong electron correlation and exchange effects, the interpretation of the frequency shift of the probed excited state relative to $2\omega_{eg}$ is less clear for molecules than in semiconductors or molecular aggregates. Despite the uncertainty about the origin of the second excited state, 2Q2D spectroscopy supplies valuable information about the properties of these excited state transitions including the relevant correlation functions and state energies. This information is important for the proper interpretation of other nonlinear spectroscopic experiments as these transitions will modulate any four-wave mixing signal due to the presence of excited state absorption (ESA). One particularly interesting question is the correlation of the transition frequency fluctuations of *different* electronic states.

An area where 2Q2D electronic spectroscopy shows great potential lies in the field of molecular aggregates. For these systems, one usually employs the two-level Frenkel exciton model to describe the electronic structure.¹¹ According to this model, the coupled chromophores give rise to an excited state with a wave function that can be written as a product of single excitations of the monomer. This model readily explains the strong ESA feature slightly blueshifted relative to the ground state bleach (GSB) in light harvesting complexes,^{22,23} whereas the monomer only shows a broad, weak, and featureless ESA.^{24,25} Theoretical studies in a protein-pigment complex using the two-level Frenkel exciton model have shown that the 2Q2D spectrum is dominated by signals originating from two-exciton states with a large delocalization length and thus can be used to probe the correlation between excited states.⁹

However, describing the monomer by a three-level system, i.e., including an excited state with a transition energy close to twice the GSB, has important consequences for the electronic structure of the aggregate. In the two-level Frenkel exciton model, there is no relaxation between the two- and one-exciton manifolds since the two-exciton states are formed as products of single excitations in the site basis^{11,23} (i.e., the two-exciton state will decay with the single exciton lifetime). The presence of a state with twice the energy of the first excited state in the monomer alters the two-exciton wave function of the aggregate by mixing in of the doubly excited molecular wave function. This opens up a relaxation pathway via internal conversion from the two-exciton band down to the first exciton manifold²⁶ and the spectral position and degree of mixing will control the rate of relaxation in these systems. It is thus important to characterize electronic states with approximately twice the energy of the GSB for the constituent pigments in order to understand the dynamics of molecular aggregates.

Similar to experiments in inorganic semiconductors, 2Q2D spectroscopy is a promising tool for the determination of the two-exciton binding energy and the delocalization of the two-exciton states in molecular aggregates. However, from the discussion above, it is clear that detailed information about the electronic structure of the constituent pigments is needed for such studies. Accordingly, it is important to experimentally and theoretically investigate the basic properties of this technique using a simple molecule and study how to extract the energies of the probed excited states from

experiments. By further analyzing the line shape of the 2Q2D spectrum, it becomes possible to address the correlation of the transition frequency fluctuation of the participating transitions. It becomes evident from the above considerations that several hitherto unknown problems including the choice of two- versus three-level monomer excitation schemes, electron-phonon couplings, and the nature of excitation dipole fluctuations dramatically affect electron-electron correlations of molecular double excitations or two-exciton band structures in molecular aggregates. The special signatures imprinted onto the coherent signal in 2Q2D spectroscopy by the abovementioned effects are puzzling and are the key issue to be studied in this contribution. This paper is organized as follows. Section II describes the experimental setup and the data evaluation procedure for measurements of S_I , S_{II} , and S_{III} signals. The experimental results obtained for Rhodamine 6G are discussed in Sec. III. Section IV is concerned with the theoretical description of the different signals with particular emphasis placed on the 2Q2D experiment under various approximations. In Sec. V, we discuss the simulations of the 1Q2D and 2Q2D experiments and how to obtain properties of the probed excited states like excited state transition dipole moments, state energies, relative detunings, and correlation functions. Finally, Sec. VI summarizes the experimental and theoretical results and discusses the utility of the 2Q2D experiments on molecules and more complicated systems.

II. EXPERIMENTAL

A. Setup

As outlined in detail previously,²⁷ our laser system consists of a regeneratively amplified Ti:sapphire system, which pumps a noncollinear optical parametric amplifier²⁸ at a repetition rate of 200 kHz. The pulses are compressed with a combination of Brewster-angle chirped mirrors²⁹ and a pair of fused silica prisms to yield a pulse duration of 23 fs at a center frequency of $19\,050\text{ cm}^{-1}$ [$\Delta=860\text{ cm}^{-1}$ FWHM (full width at half maximum)].

In order to retain amplitude- and phase-information, the time delay that is Fourier transformed in the data evaluation procedure needs to be precisely set and kept stable. To achieve this required phase stability between the three excitation pulses and the local oscillator used for heterodyne detection, we have implemented a passively phase-stabilized setup based on a diffractive optical element³⁰ (Fig. 2). Since recording 1Q2D spectra and 2Q2D spectra requires different time delays to be Fourier transformed, the diffractive optical element (DOE) consists of two transmission gratings with a groove spacing of $15\text{ }\mu\text{m}$ that are both optimized for diffraction into \pm first order. By orienting these two gratings perpendicular to each other, four phase-stable pulses in a boxcar geometry are obtained.³¹ The DOE is oriented at an angle of 45° with respect to the optical table so that the square formed by the four pulses is also tilted by 45° . The four pulses pass through a hole in the spherical mirror (SM1) and are reflected from a plane mirror (M1) back onto SM1. This arrangement allows one to implement the spherical mirror under an angle of 0° . SM1 parallelizes the four beams which

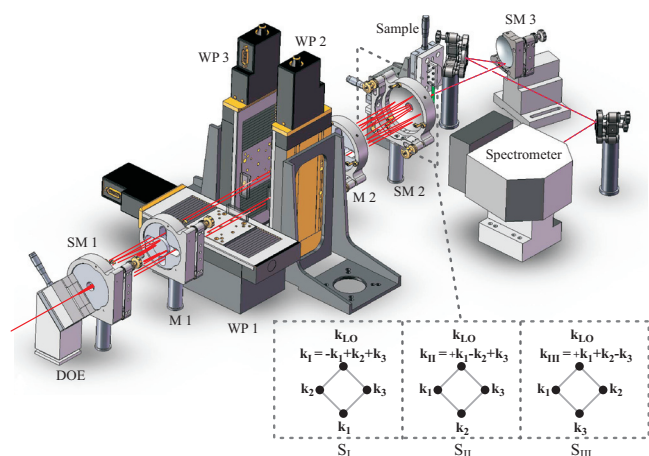


FIG. 2. Experimental design for recording 1Q2D and 2Q2D electronic spectra. Four phase-stable pulses are generated by a DOE. Three of them can be individually delayed by pairs of glass wedges (WP1–WP3) mounted on computer controlled delay stages. SM—spherical mirror; M—plane mirror. An assignment of the four pulses in the three different methods is shown in the inset. Depending on the method, the labeling of the pulses differs and does not correspond to the labeling of the wedge pairs.

pass by M1 on the top, bottom, right, and left sides. Three pairs of glass wedges (WP1–WP3) mounted on computer controlled delay stages allow one to introduce delays with a precision of ≈ 5 as in all three excitation pulses.³² Two of these delay stages (WP2 and WP3) are mounted on 90° angle brackets, i.e., perpendicular to the optical table, which ensures that no wedge clips another beam during movements. The maximum delay achievable with this configuration without introducing a notable amount of chirp is ± 800 fs as checked by a separate ZAP-SPIDER (zero additional phase spectral phase interferometry for direct electric field reconstruction) measurement.³⁰ After the delay stages, an identical plane (M2) and a spherical mirror (SM2) configuration focuses all four beams to a common spot size of ≈ 200 μm in the sample.

The third-order signal induced in the sample by the three excitation pulses propagates collinearly with the local oscillator pulse, which is attenuated by a neutral density filter (not plotted in Fig. 2) and passes through the sample ≈ 540 fs before the other pulses. This value is confirmed by an interferometric measurement involving a 25 μm pinhole as discussed below. The signal and the local oscillator (LO) are spatially filtered from the excitation pulses and are focused by SM3 onto the entrance slit of a spectrometer consisting of a grating as the dispersive element and a 1024 pixel photodiode array.

B. Data acquisition and evaluation

The points of zero delay between the excitation pulses are determined by spectral interferometry on a daily basis. Additionally, prior to each measurement series, a calibration coefficient to convert the movement of the glass wedges (in motor steps) into the actually introduced delay has to be determined for each stage separately. Accurate determination of this conversion factor is crucial in the evaluation procedure since it influences the position of the peak along the

frequency axis obtained from Fourier transform of the scanned time delay (i.e., ω_1 in 1Q2D and ω_2 in 2Q2D spectroscopy).

Since the signal and the LO have to coincide spatially in all three methods discussed in this contribution, the assignment of the beams differs for S_I , S_{II} , and S_{III} , as illustrated in Fig. 2, and does not correspond to the labeling of the wedge pairs. The beam interacting with the negative sign is thereby opposite to the LO in all three cases (i.e., \mathbf{k}_1 in S_I , \mathbf{k}_2 in S_{II} , and \mathbf{k}_3 in S_{III} , respectively).

To obtain absorptive real parts and dispersive imaginary parts in 1Q2D electronic spectra, rephasing (S_I) and non-rephasing (S_{II}) signal parts have to be equally weighed.^{7,33} For collecting S_I -spectra, t_1 (i.e., the delay between the first two excitation pulses) is scanned from 0 to 100 fs in steps of 0.5 fs by moving WP1. S_{II} -spectra are recorded by scanning WP3 and thereby delaying \mathbf{k}_1 from 0 to 100 fs. The delay between the second and the third excitation pulses (t_2) is fixed to a certain value before each scan by moving WP2. For recording 2Q2D electronic spectra, pulses 1 and 2 are scanned simultaneously from 0 to -100 fs in steps of 0.25 fs by moving WP2 and WP3 for a fixed value of t_1 . The step-size of 0.5 fs for 1Q2D spectra and 0.25 fs for 2Q2D spectra, respectively, is sufficient for fulfilling the Nyquist sampling criterion. Decreasing the step-size further does not improve the data quality as illustrated in Appendix A.

Before each scan, the scattering contribution of pulse 3 into the direction of \mathbf{k}_s is recorded by blocking pulses 1 and 2. This contribution has to be recorded and subtracted only once since the delay between pulse 3 and the LO does not change in the course of one scan. The scattering contribution of pulses 1 and 2, on the other hand, is recorded and subtracted from the spectral interferogram for each measuring point by blocking pulse 3 with an automated shutter.

Data evaluation follows the procedure outlined by Gallagher *et al.*³⁴ and Brixner *et al.*³⁵ In the first step, the spectral amplitude and the phase of the signal field are extracted from the heterodyned signal by Fourier transform, filtering of the signal components at zero and negative delays, and back Fourier transform. In the second step, the dataset is zero-padded (to increase the resolution) and Fourier transformed along t_1 to yield the frequency axis ω_1 in case of 1Q2D electronic spectroscopy or along t_2 to yield the frequency axis ω_2 in case of 2Q2D electronic spectroscopy. Finally, the absolute phase of the complex valued spectrum has to be determined. For 1Q2D spectra, this can be done by applying the projection-slice theorem, which states that the projection of the 1Q2D signal onto ω_3 equals the spectrally resolved pump-probe spectrum recorded for the same delay t_2 .⁵ Since the pump-probe signal is invariant to constant phase shifts of either the pump or the probe beam, the absolute phase can be determined in a procedure termed phasing by searching for the phase that minimizes the difference between the projection of the 1Q2D spectrum and the spectrally resolved pump-probe signal.

Determining the absolute phase of 2Q2D spectra requires a different approach since no straightforward connection exists between the 2Q2D signal and an auxiliary measurement such as pump-probe spectroscopy. Bristow *et al.*³⁶

demonstrated an all-optical method, which is a combination of spatial interference patterns and spectral interferometry, for the retrieval of the absolute phase. Backus *et al.*³⁷ reported on a spectral interferometry based method for obtaining the desired value. Moran *et al.*³⁸ determined the LO-delay by assuming that the heterodyne transient grating signal from the pure solvent has dispersive properties only. We adopted a different approach that relies on the high phase stability of our setup.³⁰ Immediately before or after recording a 2Q2D spectrum, we measured a 1Q2D spectrum and determined its absolute phase by phasing with a pump-probe spectrum. This value of the absolute phase and delay between the signal and LO is then applied to phase the 2Q2D spectrum. Possible error sources in the present phasing procedure and implications of an incorrect phasing are discussed in Appendix A.

C. Sample

Rhodamine 6G solutions with a concentration of 1.7×10^{-4} M were prepared with spectrophotometric grade ethanol (Sigma-Aldrich, www.sigma-aldrich.com). To avoid signals from cell windows, we have implemented a gravity-driven wire-guided drop jet for sample circulation^{39,40} yielding a film of ≈ 200 μm thick ($\text{OD}_{\text{max}}=0.35$). No photodegradation was observed during the course of the measurements for the employed pulse energy of 3 nJ, corresponding to a fluence of 1.44×10^{14} photons/ cm^2 or an excitation of 2.24% of the molecules in the sample volume.

III. EXPERIMENTAL RESULTS

Figures 3(a) and 3(b) display rephasing (S_I) and nonrephasing (S_{II}) 1Q2D electronic spectra for Rhodamine 6G. The real and imaginary parts show the typical characteristics of rephasing and nonrephasing 1Q2D spectra of a simple chromophore. The spectra and the nodal lines are directed along the diagonal (antidiagonal) for the rephasing (nonrephasing) spectrum. In the real part of the total 1Q2D spectrum $[S_I+S_{II}]$, Fig. 3(c), we find a strong positive feature stemming from GSB and stimulated emission (SE) and a weak, redshifted negative feature arising from ESA at $\omega_3 = 18\,200$ cm^{-1} . The elongation of the total 1Q2D spectrum along the diagonal indicates spectral inhomogeneity on the timescale of the experiment.^{41,42} Extending the measurement to longer t_2 values reveals the presence of spectral diffusion as the spectrum acquires a more circular shape (data not shown).

The 2Q2D electronic spectrum of Rhodamine 6G, separated into real and imaginary parts, is plotted in Fig. 4. Since the system evolves in a double-quantum coherence during t_2 , the features appear at approximately twice the single-quantum frequency ω_{eg} along ω_2 . The 2Q2D technique probes nonrephasing Feynman pathways (Fig. 1) and the real part of the 2Q2D signal shows similarities to the S_{II} technique with respect to the direction of the spectrum [compare to Fig. 3(b)]. For the 2Q2D technique, causality ensures that no signal is generated in the $+\mathbf{k}_1+\mathbf{k}_2-\mathbf{k}_3$ direction for $t_2 < 0$ and $t_3 < 0$. This implies that the 2Q2D spectrum only involves a half-sided Fourier transform that results in phase-

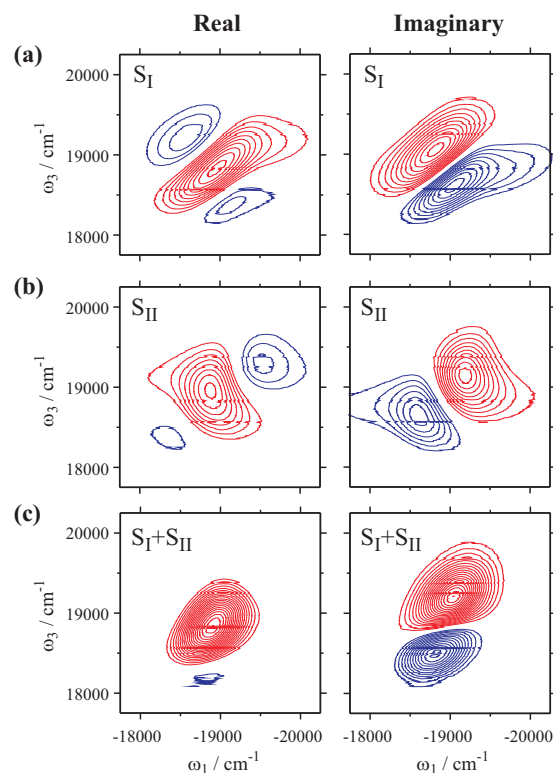


FIG. 3. 1Q2D spectra of Rhodamine 6G for $t_2=0$ separated into real (left) and imaginary (right) part. (a) S_I -technique (rephasing 1Q2D). (b) S_{II} -technique (nonrephasing 1Q2D). (c) The sum of these two spectra yields an absorptive real part and a dispersive imaginary part. Contour lines are drawn in steps of 5%, starting at 10% signal intensity. Positive (negative) features are drawn in red (blue). The S_I and S_{II} spectra are drawn with their relative contributions to the 1Q2D (S_I+S_{II}) spectra, which are normalized to their respective maximum absolute value.

twisted line shapes (cf. Sec. IV A). Causality also affects the S_I and S_{II} techniques, and it is firmly established that the real parts of S_I and S_{II} spectra display negative components already for a two-level system.⁷ These stem from the dispersive parts of the optical response and they cancel when S_I and S_{II} spectra are added together, giving absorptive line shapes for the real part of 1Q2D measurements (S_I+S_{II}).⁷ Beyond the homogeneous limit, a balancing of S_I and S_{II} spectra is not sufficient to ensure absorptive signals since strong system-bath interactions and a finite Stokes shift also give rise to negative components in 1Q2D spectra.⁴³ Our experimental results reveal strong negative features in our S_I and S_{II} spectra [Figs. 3(a) and 3(b)] that almost disappear in the total 1Q2D spectrum [Fig. 3(c)]. This illustrates the danger of techniques involving half-sided Fourier transforms. In these techniques, it is not generally possible to use the sign of a specific feature to assign it to a specific Feynman pathway as can be done for 1Q2D spectra.⁴⁴ Even in the homogeneous limit, there is no possibility to construct absorptive line shapes for 2Q2D spectra within third-order nonlinear spectroscopy, and there is consequently no unique connection between the sign of a feature in the 2Q2D spectrum and the sign of the response function. We argue that the presence of more than two peaks in the 2Q2D spectrum reflects the phase-twisted line shapes of the signals in this experiment. Neglecting the weaker negative feature for a moment, the main negative peak in the 2Q2D spectrum is located at

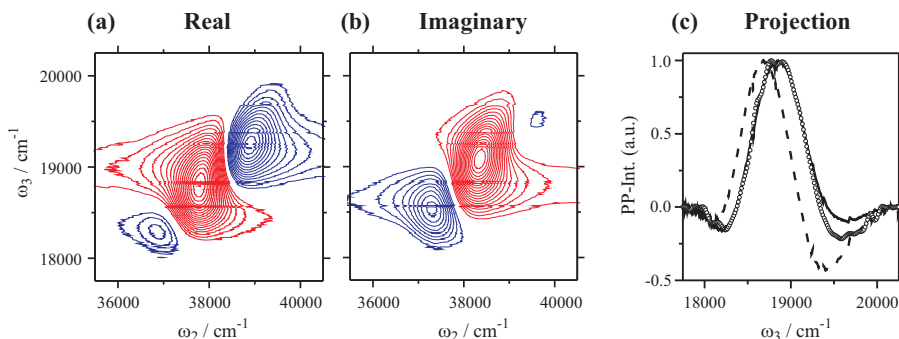


FIG. 4. (a) Real and (b) imaginary parts of the 2Q2D spectrum of Rhodamine 6G for $t_1=0$. Contour lines are drawn in steps of 5%, starting at 10% signal intensity. Positive (negative) features are drawn in red (blue). The spectra are normalized to their respective maximum absolute value. (c) Projections of the real part of the 1Q2D spectrum (solid) and the 2Q2D spectrum (dashed) onto the ω_3 -axis as compared to a spectrally resolved pump-probe spectrum (circles).

higher frequencies along ω_3 compared to the positive one. Using a simplistic interpretation based on the Feynman diagrams (Fig. 1), one would interpret this as a blueshift of the ESA relative to GSB. This is in contradiction with the results obtained by the 1Q2D spectra, where the ESA contribution is redshifted compared to GSB and SE, and additional theoretical investigations are needed to interpret the 2Q2D spectrum.

IV. THEORY

To understand the appearance of 2Q2D spectra and the relation to 1Q2D spectra, we consider an electronic three-level system coupled to a heat bath. The central quantity in third-order nonlinear spectroscopy is the third-order polarization,⁶

$$P^{(3)}(\mathbf{r}, t) = \int_{-\infty}^{\infty} \int_{-\infty}^{\infty} \int_{-\infty}^{\infty} dt_3 dt_2 dt_1 E(\mathbf{r}, t - t_1) E(\mathbf{r}, t - t_1 - t_2) \times E(\mathbf{r}, t - t_1 - t_2 - t_3) R^{(3)}(t_1, t_2, t_3), \quad (1)$$

where the response functions are given by

$$R^{(3)} = \left(\frac{i}{\hbar} \right)^3 \langle \langle \mu | G(t_3) \mathcal{V} G(t_2) \mathcal{V} G(t_1) \mathcal{V} | \rho(-\infty) \rangle \rangle. \quad (2)$$

Here, μ is the transition dipole moment operator, \mathcal{V} is the Liouville space transition dipole moment superoperator, and $G(t)$ are Liouville space Green's functions. Both the (time independent) transition dipole moment (super) operator and the Green's functions depend on the particular model and level structure. For the remainder of this paper, we will consider a three-level system with energy levels $|g\rangle$, $|e\rangle$, and $|f\rangle$, where the $|g\rangle \rightarrow |e\rangle$ and $|e\rangle \rightarrow |f\rangle$ transitions have comparable energies.

The potential energy surfaces along an effective nuclear coordinate q for this system are shown in Fig. 5. For this model, there are only two unique pathways that are accessible in the 2Q2D experiment. The corresponding Feynman diagrams are shown in Fig. 1(c), and the corresponding four point correlation functions read as

$$\begin{aligned} R^{(2Q2D)} &= R_{4f} - R_{3f}^* \\ &= \langle \langle \mu_{eg} | G_{eg}(t_3) \mathcal{V}_{eg,fg} G_{fg}(t_2) \mathcal{V}_{fg,eg} G_{eg}(t_1) \mathcal{V}_{eg,gg} | \rho_{gg}(-\infty) \rangle \rangle \\ &\quad - \langle \langle \mu_{fe} | G_{fe}(t_3) \mathcal{V}_{fe,fg} G_{fg}(t_2) \mathcal{V}_{fg,eg} G_{eg}(t_1) \\ &\quad \times \mathcal{V}_{eg,gg} | \rho_{gg}(-\infty) \rangle \rangle \end{aligned}$$

$$\begin{aligned} &= |\mu_{eg}|^2 |\mu_{fg}|^2 [\langle \langle G_{eg}(t_3) G_{fg}(t_2) G_{eg}(t_1) | \rho_{gg}(-\infty) \rangle \rangle \\ &\quad - \langle \langle G_{fe}(t_3) G_{fg}(t_2) G_{eg}(t_1) | \rho_{gg}(-\infty) \rangle \rangle]. \end{aligned} \quad (3)$$

A. Double-quantum two-dimensional signal in the homogeneous limit

To illustrate the spectral line shapes obtained in the 2Q2D experiment, we derive closed form expressions for the response function $R^{(2Q2D)}$ in Eq. (3). If the bath has a short correlation time, we may apply the homogeneous (motional narrowing) limit where the average over the four point correlation function factorizes into averages over the individual propagators.⁶ For R_{4f} , we obtain

$$\begin{aligned} \langle \langle G_{eg}(t_3) G_{fg}(t_2) G_{eg}(t_1) | \rho(-\infty) \rangle \rangle \\ \approx \langle \langle G_{eg}(t_3) | \rho(-\infty) \rangle \rangle \langle \langle G_{fg}(t_2) | \rho(-\infty) \rangle \rangle \langle \langle G_{eg}(t_1) | \rho(-\infty) \rangle \rangle. \end{aligned} \quad (4)$$

The averaged Green's function in the Bloch approximation reads as⁶

$$\langle \langle G_{mn}(t) | \rho(-\infty) \rangle \rangle = \theta(t) \exp(-\Gamma_{mn}) \exp(-i\omega_{mn}t), \quad (5)$$

where $\omega_{mn} = (1/\hbar)(E_m - E_n)$, Γ_{mn} is a dephasing rate, and $\theta(t)$ is the step function reflecting the causality of the response. The propagator and Eq. (5) can be Fourier transformed using standard formulas. Applying the homogeneous limit to R_{4f}

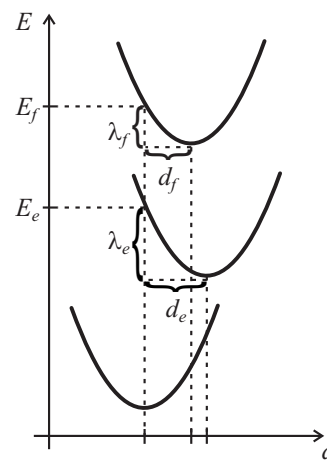


FIG. 5. Potential energy surfaces for the $|g\rangle$, $|e\rangle$, and $|f\rangle$ states. The dimensionless displacements along the effective nuclear coordinate q are denoted by d_e and d_f . The corresponding reorganization energies (λ_e and λ_f) are indicated in the figure. The energies of the levels (denoted by E_e and E_f) refer to the vertical transition energies.

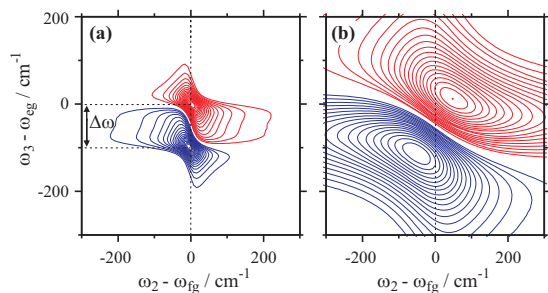


FIG. 6. 2Q2D spectra in the impulsive limit invoking the homogeneous limit and the Bloch approximation. (a) $\Delta\omega = 100 \text{ cm}^{-1}$ and $\Gamma = 25 \text{ cm}^{-1}$. (b) $\Delta\omega = 100 \text{ cm}^{-1}$ and $\Gamma = 125 \text{ cm}^{-1}$. Contour lines are drawn on a linear scale with 5% increments. Red (blue) lines refer to positive (negative) contributions.

and R_{3f}^* [Eq. (4)] and taking the Fourier transform of the propagators in Eq. (5) along ω_2 and ω_3 , we obtain the real part of the 2Q2D spectrum in the impulsive limit as

$$S^{(2Q2D)}(\omega_2, \omega_3) = \frac{\mu_{fe}^2 \mu_{eg}^2}{(\omega_2 - \omega_{fg})^2 + \Gamma_{fg}^2} \left\{ \frac{\Gamma_{eg} \Gamma_{fg} - (\omega_3 - \omega_{eg})(\omega_2 - \omega_{fg})}{(\omega_3 - \omega_{eg})^2 + \Gamma_{eg}^2} - \frac{\Gamma_{fe} \Gamma_{fg} - (\omega_3 - \omega_{fe})(\omega_2 - \omega_{fg})}{(\omega_3 - \omega_{fe})^2 + \Gamma_{fe}^2} \right\}. \quad (6)$$

Equation (6) highlights some of the properties of the 2Q2D spectrum in the homogeneous limit. Assuming that all dephasing rates are identical, the signal in the homogeneous limit vanishes if $\omega_{eg} = \omega_{fe}$. Furthermore, it is clear from Eq. (6) that the term corresponding to R_{4f} (R_{3f}^*) is not strictly positive (negative). This is directly analogous to the phase-twisted line shapes in rephasing (S_I) and nonrephasing (S_{II}) 1Q2D spectra.⁷ From the Feynman diagrams in Fig. 1, it is obvious that 2Q2D spectroscopy is a nonrephasing technique, and Eq. (6) predicts a spectrum that is elongated along the antidiagonal.^{7,10,45} Figure 1 compares the real parts of the S_I , S_{II} , and S_{III} techniques for the model discussed above, highlighting the strong similarities between the S_{II} and the S_{III} techniques originating in the nonrephasing character of these experiments. Neither the direction of the spectrum nor the phase-twisted line shapes are related to our particular choice of Green's functions or the application of the homogeneous limit discussed above, but reflect the properties of the four point correlation functions and causality of the optical response.

Figure 6(a) shows the 2Q2D spectrum calculated via Eq. (6) for the case where $|\Delta\omega| > \Gamma$ ($\Delta\omega = \omega_{eg} - \omega_{fe}$). The signal is elongated along the antidiagonal and shows two peaks of different signs corresponding to the two response functions R_{4f} and R_{3f}^* . The two peaks are centered at the same ω_2 and displaced by $\Delta\omega$ along ω_3 . This case corresponds to the narrow linewidth limit where the linewidth of each transition is smaller than the splitting between them. In this narrow linewidth limit, the 2Q2D spectrum can be interpreted with simple arguments related to the double-sided Feynman diagrams shown in Fig. 1. Turning to the opposite case [$\Delta\omega < \Gamma$, cf. Fig. 6(b)], we find that the 2Q2D spectrum changes its appearance substantially. The two main peaks are

no longer aligned at the same ω_2 and they move further apart as Γ increases. The same trend holds for the position of the peaks along ω_3 . In case the linewidth is comparable to or larger than the splitting of the states, the energy difference between the positive and the negative peaks in the 2Q2D spectrum is no longer a good indicator of $\Delta\omega$.

This example shows that the overlap of the two contributing pathways can drastically change the appearance of the 2Q2D spectrum. Electronic transitions of molecules in solution typically exhibit a strong coupling to the environment and the total reorganization energy of all modes is of the order of 500–1000 cm^{-1} . It is clear that the narrow linewidth limit is never valid for solvated molecules and we expect that the influence of the overlap of the two response functions is critical for understanding the 2Q2D spectrum. However, comparing the experimental results (Fig. 4) with the simulations in Fig. 6, it is obvious that the homogeneous limit cannot explain the experimental results even for an arbitrary line shape function. The simulations in the homogeneous limit fail to account for the number of peaks in the 2Q2D spectrum as well as the different appearance of the negative feature in 1Q2D and 2Q2D spectra.

B. Double-quantum two-dimensional signals within the cumulant expansion

The homogeneous limit does not allow for any correlation of the bath fluctuations for different time periods. This level of theory thus cannot account for the Stokes shift. In order to incorporate correlations of transition frequency fluctuations between different periods and for an arbitrary line shape as well as finite Stokes shift, we use the second-order cumulant expansion⁶ to express the four point correlation functions in terms of line shape functions. The relevant response functions have been derived elsewhere,^{35,46,47} so we quote the results important for the double-quantum coherence response functions in our analysis, namely,

$$R_{4f} = (|\mu_{eg}| |\mu_{fe}|)^2 \exp\{i(\omega_{eg}t_1 + \omega_{fg}t_2 + \omega_{eg}t_3)\} \times \exp\{-g_{ee}(t_1) + g_{ef}(t_1) - g_{ee}(t_2) + 2g_{ef}(t_2) - g_{ff}(t_2) - g_{ee}(t_3) + g_{ef}(t_3) + g_{ee}(t_1 + t_2) - g_{ef}(t_1 + t_2) + g_{ee}(t_2 + t_3) - g_{ef}(t_2 + t_3) - g_{ee}(t_1 + t_2 + t_3)\} \quad (7)$$

and

$$R_{3f}^* = (|\mu_{eg}| |\mu_{fe}|)^2 \exp\{i(\omega_{eg}t_1 + \omega_{fg}t_2 + \omega_{fe}t_3)\} \times \exp\{-g_{ee}(t_1) + g_{ef}(t_1) + g_{ee}(t_2) - g_{ef}(t_2) - g_{ee}^*(t_3) + g_{ef}^*(t_3) - g_{ee}(t_1 + t_2) - g_{ee}(t_2 + t_3) + 2g_{ef}(t_2 + t_3) - g_{ff}(t_2 + t_3) + g_{ee}(t_1 + t_2 + t_3) - g_{ef}(t_1 + t_2 + t_3)\}. \quad (8)$$

Here, $g_{ab}(t)$ are complex line shape functions defined as

$$g_{ab}(t) = \int_0^t d\tau_1 \int_0^{\tau_1} d\tau_2 C_{ab}(\tau_2), \quad (9)$$

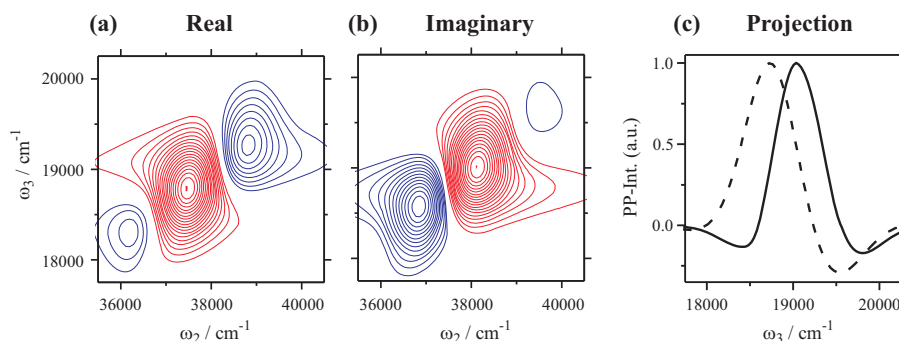


FIG. 7. (a) Real and (b) imaginary parts of the simulated 2Q2D spectrum. Contour lines are drawn on a linear scale with 5% increments starting from the 10% level. Red (blue) lines refer to positive (negative) contributions. (c) Projection of the 1Q2D spectrum (solid) and 2Q2D spectrum (dashed) onto the ω_3 -axis.

$$C_{ab}(t) = \frac{1}{\hbar^2} \langle \Delta W_{ag}(t) \Delta W_{bg}(0) \rangle, \quad (10)$$

where $C_{ab}(t)$ is the energy gap correlation function and $\Delta W_{ag} = W_a(q) - W_g(q) - \langle W_a(q) - W_g(q) \rangle$ is the energy gap operator. The response functions involving the $|f\rangle$ -level depend on three correlation functions since we have chosen to set the ground state as a reference potential energy surface. Their mutual relations depend on the particular character of the bath. In a single Brownian mode model depicted in Fig. 5, rather strict relations apply. The bath interacts with the electronic transition through a single effective coordinate q that couples to both the rest of the bath and the electronic transition. The displacement of the effective mode in the electronic state a ($a=e, f$) is d_a . The time evolution of the energy gap operator is given by⁶

$$\Delta W_{ag}(t) = U_g^*(t) \Delta W_{ag} U_g(t) = \hbar \omega_a d_a U_g^*(t) q U_g(t), \quad (11)$$

where $U_g(t)$ is the nuclear time evolution operator corresponding to the electronic ground state. More information on the energy gap correlation functions for an electronic three-level system is provided in Appendix B. Here, we elaborate on the simplest case where the bath can be described by a single Brownian oscillator mode.

For a single harmonic nuclear coordinate, the three energy gap correlation functions read as

$$C_{ab}(t) = \omega_a \omega_b d_a d_b \langle q(t) q \rangle. \quad (12)$$

Here, $\langle q(t) q \rangle$ is the autocorrelation function of the generalized coordinate q . The experimentally accessible quantity is the reorganization energy given by

$$\lambda_a = S_a \omega_a = \frac{1}{2} \omega_a d_a^2, \quad (13)$$

where S is the Huang–Rhys factor. Assuming that the frequency of the mode is the same in all states, we arrive at

$$C_{ab}(t) = d_a d_b c(t), \quad (14)$$

with

$$c(t) = \omega^2 \langle q(t) q \rangle. \quad (15)$$

The three correlation functions ($C_{ee}(t)$, $C_{ff}(t)$, $C_{ef}(t)$) are not independent but related to the bath induced fluctuations of the same coordinate. The magnitude of the diagonal correlation functions $C_{ee}(t)$ and $C_{ff}(t)$ depends on the displacement of the involved state (relative to the ground state) in direct analogy with the results for a two-level system. The magnitude of the cross-correlation function $C_{ef}(t)$ depends on the

displacement associated with both transitions $|g\rangle \rightarrow |e\rangle$ and $|g\rangle \rightarrow |f\rangle$. Because the displacement can be negative, an anti-correlation is also allowed.

Extending the above relation to a multimode bath of independent Brownian oscillators cf. Appendix B, one finds that

$$C_{ab} = \sum_j d_a^{(j)} d_b^{(j)} \omega_j^2 \langle q_j(t) q_j \rangle = \sum_j d_a^{(j)} d_b^{(j)} c^{(j)}(t). \quad (16)$$

In the multimode picture, the cross-correlation function is determined by the overlap of the displacement vectors $\mathbf{d}_a = (d_a^{(1)}, \dots, d_a^{(N)})$ corresponding to the two excited electronic states. A cross-correlation function $C_{ef}(t)$ of a multicomponent bath is therefore rather freely related to the self-correlation functions associated with the two transitions.

V. SIMULATIONS

For our simulations, we use a simple parametrization of the different correlation functions. We use a correlation function $C_{ee}(t)$ with vibrational modes obtained from resonance Raman experiments⁴⁸ ($\sum_j \lambda_j = 353 \text{ cm}^{-1}$) and three overdamped modes reflecting fast ($\tau_G = 40 \text{ fs}$, $\lambda_G = 150 \text{ cm}^{-1}$ and $\tau_{E_1} = 100 \text{ fs}$, $\lambda_{E_1} = 150 \text{ cm}^{-1}$) and slow ($\tau_{E_2} = 1 \text{ ps}$, $\lambda_{E_2} = 100 \text{ cm}^{-1}$) bath fluctuations, where E and G refer to Gaussian and exponential modes, respectively. This correlation function gives good agreement with the linear absorption spectrum of the $|g\rangle \rightarrow |e\rangle$ transition. In the next step, we assume that the shape of the normalized correlation function is the same for $C_{ee}(t)$ and $C_{ff}(t)$ and use the displacement of the $|g\rangle \rightarrow |f\rangle$ transition (d_f) as a free parameter. For a multicomponent bath, Eq. (16) shows that the form of $C_{ef}(t)$ is only loosely related to those of $C_{ee}(t)$ and $C_{ff}(t)$. We thus start with a single component bath model, i.e., with Eq. (14), and relax its strict prescription for $C_{ef}(t)$ if it conflicts with experimental evidence. The remaining parameters of the model are the energy of the $|g\rangle \rightarrow |f\rangle$ transition, $\omega_{fg} = \omega_{eg} + \omega_{fe}$, and the relative transition dipole moment μ_{fe}/μ_{eg} . The latter cannot be obtained from the 2Q2D experiment since both pathways depend on the same transition dipole moments [see Eq. (6)]. To estimate the magnitude of the transition dipole moments, we complement the simulations of the 2Q2D spectrum with simulations of the 1Q2D experiment at $t_2 = 0$.

Figures 7 and 8 summarize the simulations of the 2Q2D and 1Q2D experiments on Rhodamine 6G in solution. These simulations employ the finite pulse envelopes used in the

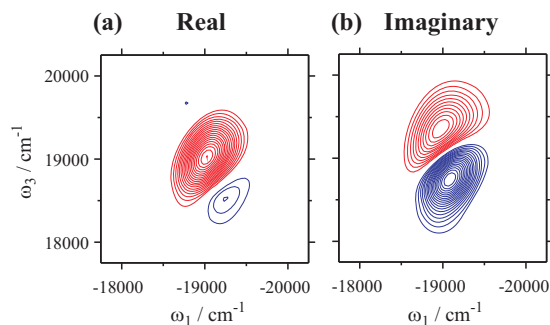


FIG. 8. (a) Real and (b) imaginary parts of the simulated 1Q2D spectrum of Rhodamine 6G for $t_2=0$. Contour lines are drawn on a linear scale with 5% increments starting from the 10% level. Red (blue) lines refer to positive (negative) contributions.

experiments and the cumulant expansion expression for the response functions. The simulations of the 2Q2D spectra in Fig. 7 are in good agreement with the experimental data in Fig. 4 and accurately capture the number of peaks, their signs, energetic positions, and relative intensities. As a consequence of the phase-twisted line shapes in 2Q2D spectra, we observe three peaks even though there are only two Feynman pathways contributing to the signal. This effect is smaller in the homogeneous limit (Fig. 6) and we find that the number of peaks and their relative intensities depend sensitively on the bath description as well as the difference between ω_{eg} and ω_{fe} . Figure 8 depicts the simulations of the real and imaginary parts of the 1Q2D spectrum in which all pulse overlap effects and the contributions from the double-quantum coherence pathways have been included. The simulations reproduce the negative contribution at low ω_3 in the real part and the two approximately equally strong features of opposite sign in the imaginary part. Finally, the simulations reproduce the energy difference between the peaks of the projection of the 1Q2D and 2Q2D spectrum onto ω_3 [cf. Fig. 7(c)].

The simulations clearly reveal that the correlation functions $C_{ee}(t)$ and $C_{ff}(t)$ have to be very similar in order to match the width of the 2Q2D spectrum. For a single component bath, this corresponds to the case where the displacements in $|e\rangle$ and $|f\rangle$ are almost the same (i.e., $d_f \approx d_e$). For the simulations of the 2Q2D spectrum alone, we find a good fit using $C_{ff}(t) = 0.9C_{ee}(t)$ if Eq. (14) is applied to obtain the cross-correlation function, i.e., $C_{ef}(t) = \sqrt{0.9}C_{ee}(t)$. Contradictory to experimental results, this choice of correlation functions gives rise to a very narrow ESA contribution in the 1Q2D spectrum. This is not surprising since the ESA pump-probe spectrum approaches a δ -function as $C_{ff}(t) \rightarrow C_{ee}(t)$.⁴⁹ Relaxing the single bath component prescription but keeping the overall shape of $C_{ef}(t)$, we find a more realistic linewidth of the ESA contribution in the 1Q2D experiment with $C_{ef}(t) = C_{ff}(t) = 0.9C_{ee}(t)$. The minor change in the magnitude of the cross-correlation function $C_{ef}(t)$ has a limited impact on the line shapes in the 2Q2D experiment and illustrates the sensitivity of different experiments to different correlation functions. The simulations thus show that the spectral distribution of the displacements $d_e(\omega)$ and $d_f(\omega)$ are similar but the average displacement is slightly less in $|f\rangle$.

Besides the different correlation functions and their rela-

tions, an important parameter determining the appearance of the 2Q2D spectrum is the energy of the $|g\rangle \rightarrow |f\rangle$ transition. This value has a profound impact on the 2Q2D spectrum with our realistic choice of correlation functions. Using Eq. (6) and Fig. 7, it is tempting to erroneously conclude that the $|e\rangle \rightarrow |f\rangle$ transition is blueshifted relative to the GSB contribution since the strongest negative component in the 2Q2D spectrum is at high ω_3 . However, this is in contrast to the 1Q2D spectrum (Fig. 8) where the ESA contribution is seen at lower ω_3 . It is difficult to understand this apparent contradiction within the homogeneous limit. The simulations in Fig. 6 with a redshifted $|e\rangle \rightarrow |f\rangle$ transition also display a redshifted negative component in the 2Q2D spectrum (and a redshift in the absorptive 1Q2D spectrum, data not shown). Compared to the simulations within the cumulant expansion (Fig. 7), it is clear that a redshifted $|e\rangle \rightarrow |f\rangle$ transition can also give rise to a negative component at high energy in the 2Q2D spectrum and a redshifted negative component in the 1Q2D spectrum. In our simulations, we accommodate these findings by a choice of $\Delta\omega = 500 \text{ cm}^{-1}$, corresponding to a redshift of the $|e\rangle \rightarrow |f\rangle$ transition relative to the GSB contribution. In general, it is not possible to extract $\Delta\omega$ directly from the 2Q2D spectrum if the system-bath interaction is strong as in the case of electronic transitions in molecules in solution.

The last parameter of the model is the relative strength of the transition dipole moments μ_{fe} and μ_{eg} . This value is difficult to estimate from experiments due to the finite bandwidth of the pulses, pulse overlap effects, and the overlap of positive and negative contributions in the 2Q2D signal. After determining the correlation functions and $\Delta\omega$ from the 2Q2D experiments, we used μ_{fe}/μ_{eg} as a parameter in the simulation of the 1Q2D spectrum. Weak negative features in the 1Q2D spectrum can result from pulse overlap effects, inertial motions, and finite Stokes shift.⁴³ We find that these effects, accounted for in our model, are too weak to explain the negative feature in the 1Q2D spectrum. Rather, the amplitude of the negative feature is controlled by the $|e\rangle \rightarrow |f\rangle$ transition dipole moment. To account for the relatively weak ESA feature seen in the experiments, we conclude that $\mu_{fe}/\mu_{eg} \leq 0.2$. The full analysis of our experiments puts our results in good agreement with the estimation of the ESA cross section made by Hammond,⁵⁰ showing an excited state with an energy of 36 000–37 000 cm^{-1} . These studies also have shown that the ESA transition has a different polarization compared to the GSB contribution. This could affect our estimation of the strength of the transition dipole moment. The mutual orientation of the transition dipole moments will be important for the interpretation of pump-probe anisotropy experiments,⁵¹ but this issue is beyond the scope of the present paper.

Figure 7(c) shows the projection of the simulated 1Q2D and 2Q2D spectra onto the ω_3 axis. The 2Q2D projection shows a clear redshift relative to the pump-probe signal (which equals the projection of the 1Q2D spectrum) and a stronger negative contribution. This also reflects the difference between the two signals seen in the experiment [Fig. 4(c)]. Considering the Liouville pathways underlying these signals (Fig. 1), there is no basis for an equivalence of these

two projections. For instance, the 2Q2D projection lacks a GSB contribution and the positive (R_{4f}) and negative (R_{3f}^*) response functions always have the same magnitude in contrast to the SE and ESA contributions in pump-probe spectroscopy. This projection can only match the pump-probe spectrum if one employs the homogeneous limit, assumes that all dephasing rates are equal, neglects the Stokes shift, and supposes that the ratio of the transition dipole moments is $\mu_{fe}/\mu_{eg}=\sqrt{2}$. Using pump-probe spectra in order to phase 2Q2D spectra directly thus lacks theoretical foundation and alternative methods must be used as discussed in Appendix A.

VI. DISCUSSION

The presence of a 2Q2D signal is an unambiguous experimental evidence for the presence of a state at roughly twice the energy of the optically allowed $|g\rangle\rightarrow|e\rangle$ transition. Analyzing the line shapes gives information about the coupling of the $|g\rangle\rightarrow|e\rangle$ and $|g\rangle\rightarrow|f\rangle$ transitions to the bath, their energies, and the transition dipole moments. However, this analysis does not give any information about the nature of the electronic excitation. For mean field models, where electron-electron correlation and exchange effects are neglected, there should be a state at twice the HOMO-LUMO energy, which can be written as the product of single excitations.¹¹ However, it is well known that the exchange and correlation terms can significantly alter the energy of electronic states in molecules. The exchange term raises the first excited state while having little impact on the doubly excited state, which is a closed shell excitation.^{16,17} This term, estimated as the singlet-triplet splitting, is of the order of 2200 cm^{-1} for Rhodamine B,²¹ and we expect it to be of the same magnitude for Rhodamine 6G. Moreover, the electron-electron correlation term in molecular systems can be substantial.⁵² Typically, this lowers the energy of the doubly excited state relative to that of the singly excited state. This effect is particularly strong in polyenes and carotenoids where the doubly excited state is lowered below the singly excited state upon inclusion of electron correlations.²⁰ In our experiment, we find that the $|e\rangle\rightarrow|f\rangle$ transition is redshifted compared to the $|g\rangle\rightarrow|e\rangle$ transition by about 500 cm^{-1} . Using a simple estimation of the singlet-triplet splitting, $\omega_{S-T}=2200\text{ cm}^{-1}$,²¹ we find that already this value is large enough to shift the doubly excited state outside the bandwidth of our laser pulses. Additionally, electron-electron correlation should further lower the doubly excited state, shifting the $|e\rangle\rightarrow|f\rangle$ transition even further. Consequently, the state we observe ($|f\rangle$) has little to do with the doubly excited state of the mean field model, and the energy of the $|e\rangle\rightarrow|f\rangle$ transition relative to the $|g\rangle\rightarrow|e\rangle$ transition should not be interpreted as the interaction (i.e., exchange and correlation) energy in this case, as has been done in previous publications.^{16,17}

The presence of an excited state at roughly twice the energy of the $|g\rangle\rightarrow|e\rangle$ transition is important for the interpretation of spectroscopic signals. The presence of an ESA contribution in the region of the GSB contribution is known for many important molecules such as chlorophylls,²⁵

bacteriochlorophylls,²⁴ and carotenoids^{44,49} and has also been shown in a large number of dyes.^{16,17} Depending on the strength, spectral position, and dynamics, these states may play a role in the analysis of the experiments of these pigments. Unless this transition is weak, the analysis of any optical experiment should take into consideration the three-level nature of the pigment when explaining the ultrafast dynamics. Recently, it was shown that to accurately account for the fast dynamics of the 1Q2D spectrum in β -carotene, it is necessary to include an ESA transition from S_2 .^{44,49} The presence of such a transition also has impact on the analysis of intensity dependence studies involving pump-probe spectroscopy.^{53,54}

We have demonstrated in the previous section that it is possible to use the 2Q2D experiment to obtain the displacement of the excited state $|g\rangle\rightarrow|f\rangle$ transition (d_f), and we found that it was very similar to the displacement of the $|g\rangle\rightarrow|e\rangle$ transition (d_e). Even though the 2Q2D pathways are of little relevance to experiments such as pump-probe outside the pulse overlap region, the correlation functions and state energies derived from this experiment determine the response functions relevant to the pump-probe ESA contribution too. These pathways generate signals with different appearance depending on d_f . If $d_f=0$, the ESA pump-probe signal will mirror the SE signal and shift to the blue as t_2 increases. If $d_f=d_e$, the pump-probe signal results in a δ -function ESA spectrum. Beyond the homogeneous limit, the dynamics of the bath gives rise to different dynamics of SE and ESA for an arbitrary displacement of $|f\rangle$. This type of information is difficult to extract directly from pump-probe spectra for two reasons. First, the overlap of three pathways contributes to the pump-probe sequence, while only two pathways contribute to the 2Q2D signal (Fig. 1). Second, the information about the energy gap correlation functions are contained both in the relaxed spectral line shape and in the change of the line shape with waiting time t_2 . Pump-probe spectra are typically analyzed in the homogeneous limit where the spectral line shape is independent of t_2 . As such, the fitting algorithms can only accurately quantify the relaxed line shape, and this information is not sufficient to unambiguously determine the energy gap correlation functions.⁵⁵

Our study indicates that the interpretation of the spectra is greatly simplified if the line shapes of the individual transitions are featureless, narrow, and display a small Stokes shift. In contrast to molecules, excitons typically interact less strongly with the bath due to their delocalized excitations, and therefore, they show rather narrow spectral line shapes.^{56,57} This situation is typically encountered in molecular dimers⁵⁸ and aggregates.^{1,27,59} For molecular aggregates, the presence of an excited state in the monomer at twice the HOMO-LUMO energy has consequences for the electronic structure and relaxation pathways in the aggregates. In the two-level Frenkel exciton model, used to interpret spectroscopy on natural and bacterial light harvesting complexes,²³ the two-exciton state wave functions are formed by a product of single excitations in the site basis. At high flux, more than one excitation can be present in the aggregate at once. As the excitons diffuse over the aggregate, they may encounter each

other and annihilate. Such a process is only possible if a state $|f\rangle$ absorbing the energy of the two excitons exists. Its presence may open a new decay channel between two- and one-exciton bands introduced by the $|f\rangle \rightarrow |e\rangle$ internal conversion, which may be much faster than the one mediated by the $|e\rangle \rightarrow |g\rangle$ transition. The spectral position of the $|e\rangle \rightarrow |f\rangle$ transition in the site basis will thus tune the decay rate of the two-exciton state and thereby the annihilation rate. This effect has been shown to control the temperature dependence of annihilation in the LH2 complex,²⁶ illustrating the importance of the spectral properties of higher excited states in these biologically relevant pigments. Clearly, 2Q2D spectroscopy could be used to select molecules with an appropriate excited state energy structure to tune the annihilation dynamics in aggregates.

VII. CONCLUSION

The ability of multidimensional spectroscopy to select specific excitation pathways by changing the order and direction of the excitation pulses makes it a versatile tool for investigation of dynamics in the condensed phase. Our newly developed setup³⁰ allows for phase-stable experiments for any time ordering of the excitation pulses. As such, we have demonstrated three different experimental techniques S_I (rephasing 1Q2D), S_{II} (nonrephasing 1Q2D), and S_{III} (2Q2D) on Rhodamine 6G in a solution. Unlike 1Q2D (i.e., $S_I + S_{II}$) spectroscopy, the 2Q2D experiment only involves pathways that propagate in a double-quantum coherence during t_2 and no direct link to auxiliary measurements such as pump-probe spectroscopy exists. To obtain the correct absolute phase of the 2Q2D spectrum, we exploit the high phase stability of the setup and use the absolute phase obtained from a 1Q2D measurement carried out directly before or after the measurement of the 2Q2D signal.³⁰

The implementation of the double-quantum coherence technique enables direct probing of excited states at twice the energy of the first optically allowed transition. Detecting a signal in this experiment provides an unambiguous experimental proof for the presence of an ESA transition within the bandwidth of the excitation pulses. This property of a 2Q2D signal is highly useful in molecules with congested electronic spectra, where the interpretation of pump-probe results can be cumbersome.⁴⁴ The 2Q2D spectrum of Rhodamine 6G reveals two main features of opposite sign directed along the antidiagonal. In addition, the spectrum reveals a second weak negative peak at lower energy. The strong positive peak is located at slightly lower frequencies than the GSB contribution (as seen in pump-probe) and the strongest negative feature is located at higher frequencies. This is found to be in contrast to the real part of the total 1Q2D spectrum where we find a weak ESA feature located at lower frequencies than the GSB signal along ω_3 . Analyzing the results in the homogeneous limit, we are able to correctly predict the direction of the spectrum but not the number of peaks nor the different appearance of the negative feature (ESA) in 1Q2D and 2Q2D spectra. To reconcile these observations, it is necessary to go beyond the homogeneous limit in the analysis of the experiments. Employing the cumulant expansion on a

three-level system coupled to a heat bath, we obtain a good fit to both the 1Q2D and 2Q2D spectra with a model including a redshifted ESA transition. Our model correctly reproduces the three peaks seen in the 2Q2D spectrum as well as their relative intensities, signs, and spectral positions. Our experiments show that the fluctuations of the two probed states ($|e\rangle$ and $|f\rangle$) relative to the ground state are strongly correlated, reflecting the modulation by a common nuclear bath and a similar nature of the electronic transitions.

Due to the strong electron-interaction (correlation and exchange) effects in this type of dye, we find that it is not possible to interpret the shift of the observed higher excited state in terms of a two-exciton binding energy. Furthermore, our results highlight the complexity of a 2Q2D spectrum for samples with strong system-bath interaction, where the overlap between the two contributing pathways has a strong impact on the spectra and leads to difficulties in their interpretation. However, we show that with proper analysis, 2Q2D spectra provide information about the energies, system-bath interactions, as well as the transition dipole moments of the probed transition. This information is needed to account for ESA contributions in other four-wave mixing experiments. Furthermore, quantifying such states may be important in molecular aggregates where they open up fast relaxation channels between the one- and two-exciton manifolds.

ACKNOWLEDGMENTS

This work was supported by the Austrian Science Foundation (FWF) within Project Nos. P22331 and F016/18 *Advanced Light Sources* (ADLIS). A.N. and J.S. thank the Austrian Academy of Sciences for partial financial support by the Doctoral Scholarship Programs (DOC-ffORTE and DOC). T.M. acknowledges the kind support by the Czech Science Foundation through Grant No. GACR 205/10/0989 and by the Ministry of Education, Youth, and Sports of the Czech Republic through Research Plan No. MSM0021620835. J.H. gratefully acknowledges support by the FWF through the Lise Meitner Project No. M1080-N16. N.C. acknowledges support from the Wenner-Gren Foundations. T.P. acknowledges support from the Swedish Research Council, STEM, and KAW.

APPENDIX A: POSSIBLE ERROR SOURCES IN RUNNING 2Q2D EXPERIMENTS

The Nyquist sampling criterion requires that a time-dependent function in which the highest contributing frequency is at x Hz needs to be sampled with a resolution better than $(1/2x)$ s (in case one is not operating in the rotating frame³¹). For 1Q2D spectra, this implies that the step-size must be no larger than ≈ 0.8 fs, whereas for 2Q2D spectra the step-size should be smaller than 0.4 fs. In our experiments, we step the relevant delays (t_1 in 1Q2D experiments and t_2 in 2Q2D experiments) by 0.5 and 0.25 fs, respectively. These step-sizes are sufficient for fulfilling the Nyquist sampling criterion and further decrease does not improve the data quality. This is illustrated in Fig. 9 where we plot the phase of the S_{III} -signal as a function of t_2 for step-sizes of 0.25 and 0.1 fs evaluated in the peak maximum

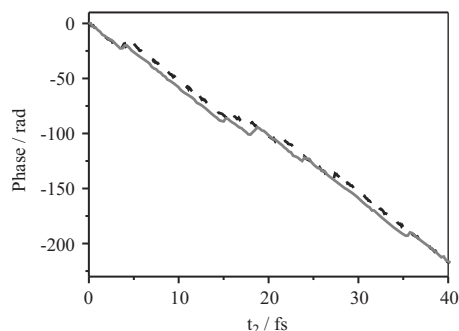


FIG. 9. Comparison of the phase of the third-order nonlinear signal detected in the phase-matched direction $+\mathbf{k}_1+\mathbf{k}_2-\mathbf{k}_3$ as a function of t_2 for step-sizes of 0.1 fs (dashed line) and 0.25 fs (solid line) evaluated at $18\,900\text{ cm}^{-1}$.

($18\,900\text{ cm}^{-1}$). A similar conclusion was also reached in a combined experimental-theoretical study investigating the effect of the sampling rate on Fourier transform spectra.⁶⁰

One critical issue in two-dimensional spectroscopy is the phasing procedure at the end of the data evaluation. Several methods have been proposed for determining the absolute phase of the complex valued 2D spectrum, which either rely on spectral interferometry^{36,37} or on the projection-slice theorem.^{34,35} In the latter, the projection of the real part of the 1Q2D signal onto ω_3 is multiplied by a phase factor so as to achieve best agreement with a spectrally resolved pump-probe spectrum.

For 2Q2D spectra, there exists no straightforward relation to an auxiliary measurement such as pump-probe spectroscopy. This is immediately obvious from inspection of the relevant Feynman diagrams (Fig. 1) for the different techniques. Therefore, one has to either resort to all-optical methods, such as demonstrated in the groups of Cundiff and Hamm,^{36,37} or exploit the phase stability of a setup and use the phase determined from a 1Q2D spectrum to phase the 2Q2D spectrum. In our measurements, we adopt the latter approach [cf. Fig. 10(b), top panel]. When applying this procedure, care has to be taken in determining the precise delay between the signal and the LO. Two values can be found that yield a reasonable agreement between the projection of the 1Q2D spectrum and the pump-probe signal [cf. Fig. 10(a)]. In case it is not obvious immediately from the inspection of the 1Q2D spectrum which value is the correct one, the delay can be determined with femtosecond precision by Fourier transforming a spectral interferogram and then fine-tuned by the phasing procedure outlined above. Taking the incorrect value for the delay between the signal and the LO for phasing the 2Q2D data set has a huge impact on the spectrum [see Fig. 10(b), bottom]. The real part of the 2Q2D spectrum retains its three-peak structure; however, the nodal line changes its orientation from parallel to the antidiagonal (as expected from a nonrephasing technique) to parallel to the diagonal line. The latter spectrum would be tempting for interpretation for two reasons: first, all peaks appear at the same frequency along ω_2 as ideally expected from the two Feynman diagrams contributing to the response (the system evolves in the same $|f\rangle\langle g|$ -coherence in both pathways). Second, one could think of extracting the shift of the double-excited state energy from twice the energy of the single-

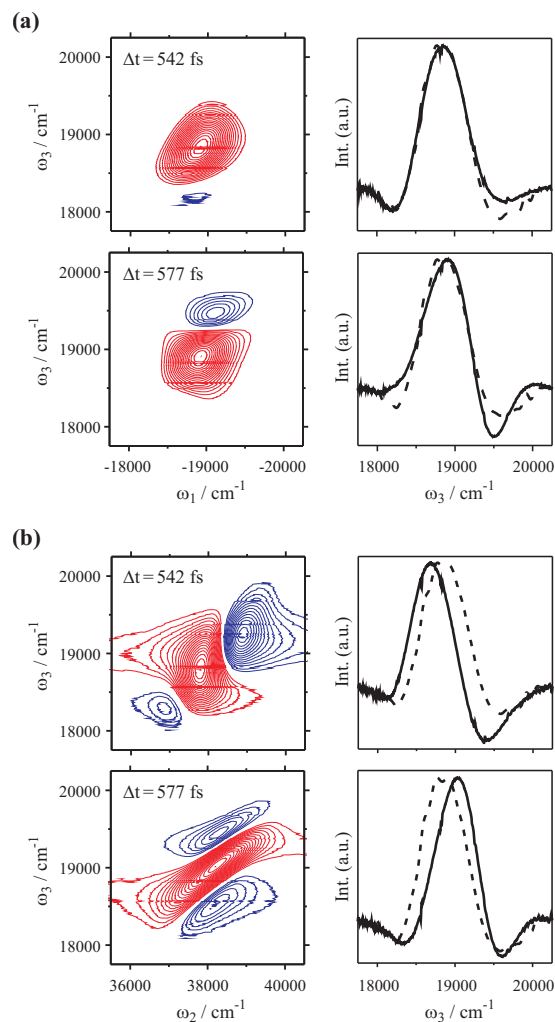


FIG. 10. Illustration of error sources in the determination of the absolute phase of 1Q2D spectra (a) and 2Q2D spectra (b). The real part of the 1Q2D spectrum (a) and 2Q2D spectrum (b) is shown on the left, their projections onto ω_3 (solid) together with a spectrally resolved pump-probe spectrum (dashed) on the right. The upper panels show the spectra for $\Delta t=542\text{ fs}$, which is the correct value also obtained via spectral interferometry. Phasing with a value of $\Delta t=577\text{ fs}$ is depicted in the lower panel.

excited state directly from the frequency difference of the positive and negative peaks along ω_3 . However, the delay between the signal and the LO deviates from the one determined by spectral interferometry by $\approx 35\text{ fs}$ in this case, which is well outside experimental errors. Furthermore, theory supports the notion of the antidiagonal orientation of the 2Q2D spectrum, as depicted in the top panel of Fig. 10(b).

APPENDIX B: SYSTEM-BATH INTERACTION IN A THREE LEVEL SYSTEM

1. Multimode bath Hamiltonian and system-bath interaction Hamiltonian

The nuclear Hamiltonian of the electronic ground state $|g\rangle$ is chosen as a reference Hamiltonian of the bath

$$H_B \equiv H_g = \sum_{k=1}^N \left(\frac{1}{2m_k} p_k^2 + \frac{m_k \omega_k^2}{2} q_k^2 \right). \quad (\text{B1})$$

Nuclear Hamiltonian operators of other electronic excited states $|e\rangle$ and $|f\rangle$ are characterized by a shift of their potential energy surfaces with respect to the ground state $|g\rangle$. Let $x = e, f$ then

$$H_x = \sum_{k=1}^N \left(\frac{1}{2m_k} p_k^2 + \frac{m_k \omega_k^2}{2} (q_k - d_x^{(k)})^2 \right). \quad (\text{B2})$$

Obviously, for $x = g$, $d_g^{(k)} = 0$ for all k .

To simplify the treatment, we introduce standard dimensionless coordinates (and momenta) as

$$\tilde{q}_k = \sqrt{\frac{m_k \omega_k}{\hbar}} q_k, \quad \tilde{p}_k = \frac{1}{\sqrt{\hbar \omega_k m_k}} p_k, \quad (\text{B3})$$

which turns the Hamiltonian in Eq. (B1) into

$$H_B = \sum_{k=1}^N \frac{\hbar \omega_k}{2} (\tilde{p}_k^2 + \tilde{q}_k^2). \quad (\text{B4})$$

From now on, we will use the dimensionless coordinates and omit tildes, i.e., we replace $\tilde{p} \rightarrow p$, $\tilde{q} \rightarrow q$, and $\tilde{d} \rightarrow d$. The nuclear Hamiltonian operators of the excited states then read as

$$H_x = H_B - \sum_{k=1}^N \hbar \omega_k d_x^{(k)} q_k + \hbar \sum_{k=1}^N \frac{\omega_k}{2} (d_x^{(k)})^2. \quad (\text{B5})$$

Each of the excited states is characterized by a reorganization energy

$$\varepsilon_{\text{reorg}}^{(x)} = \hbar \lambda_x = \hbar \sum_{k=1}^N \lambda_x^{(k)}, \quad (\text{B6})$$

and an electron-phonon interaction Hamiltonian

$$H_x^{(\text{int})} = \Delta W_{xg} |x\rangle \langle x| = -\hbar \sum_{k=1}^N \omega_k d_x^{(k)} q_k |x\rangle \langle x|. \quad (\text{B7})$$

A widely used dimensionless quantity that characterizes the electron-phonon coupling is the Huang–Rhys factor

$$S_x^{(k)} = \frac{\lambda_x^{(k)}}{\omega_k} = \frac{1}{2} (d_x^{(k)})^2. \quad (\text{B8})$$

Its main advantage is that it is defined by experimentally available quantities $\lambda_x^{(k)}$ and ω_k .

2. Equivalence of the effective Brownian coordinate and multimode bath models

Often, instead of Eq. (B2), the bath Hamiltonian operators are assumed in the form

$$H_x = \frac{\hbar \omega_0}{2} \left[p_0^2 + \left(q_0 - d_x^{(0)} - \sum_{\alpha=1}^N \kappa_{\alpha} q_{\alpha} \right)^2 \right] + \sum_{\alpha=1}^N \frac{\hbar \omega_{\alpha}}{2} (p_{\alpha}^2 + q_{\alpha}^2), \quad (\text{B9})$$

which corresponds to the case of a single effective coordinate q_0 coupled to the electronic transition (through displacement $d_x^{(0)}$) and to a bath of oscillators that are not coupled to the electronic transition directly. By expanding the square in the first term, we obtain

$$H_x = \frac{\hbar \omega_0}{2} (p_0^2 + q_0^2) + \hbar \lambda_x - \hbar \omega_0 d_x^{(0)} q_0 - \hbar \omega_0 \sum_{\alpha=1}^N \kappa_{\alpha} q_{\alpha} q_0 + \frac{\hbar \omega_0}{2} \sum_{\alpha\beta} \kappa_{\alpha} \kappa_{\beta} q_{\alpha} q_{\beta} + \sum_{\alpha=1}^N \frac{\hbar \omega_{\alpha}}{2} (p_{\alpha}^2 + q_{\alpha}^2) + \hbar \omega_0 \sum_{\alpha=1}^N \kappa_{\alpha} q_{\alpha} d_x^{(0)}, \quad (\text{B10})$$

where $\lambda_x = \omega_0 (d_x^{(0)})^2 / 2$ is the reorganization energy. The first term on the second line of Eq. (B10) corresponds to the bilinear interaction between modes α and β . To account for such an interaction, we can transform the coordinates to a new set of normal modes defined as $\tilde{q}_{\alpha} = \sum_{\gamma} \tilde{C}_{\gamma}^{(\alpha)} q_{\gamma}$ such that the interaction term disappears. By this transition, we obtain new mode frequencies $\tilde{\omega}_{\alpha}$ and new couplings $\tilde{\kappa}_{\alpha}$ of the normal modes to the mode q_0 . Equation (B10) turns into

$$H_x = \frac{\hbar \omega_0}{2} (p_0^2 + q_0^2) + \hbar \lambda_x - \hbar \omega_0 d_x^{(0)} q_0 - \hbar \omega_0 \sum_{\alpha=1}^N \tilde{\kappa}_{\alpha} \tilde{q}_{\alpha} q_0 + \sum_{\alpha=1}^N \frac{\hbar \tilde{\omega}_{\alpha}}{2} (\tilde{p}_{\alpha}^2 + \tilde{q}_{\alpha}^2) + \hbar \omega_0 \sum_{\alpha=1}^N \tilde{\kappa}_{\alpha} \tilde{q}_{\alpha} d_x^{(0)}. \quad (\text{B11})$$

The last term can be included into the quadratic form of the Hamiltonian of the \tilde{q}_{α} modes by defining $\bar{q}_{\alpha} = \tilde{q}_{\alpha} + \tilde{\kappa}_{\alpha} (\omega_0 / \tilde{\omega}_{\alpha}) d_x^{(0)}$, which yields

$$H_x = \frac{\hbar \omega_0}{2} (p_0^2 + q_0^2) + \hbar \bar{\lambda}_x - \hbar \omega_0 \bar{d}_x q_0 + \sum_{\alpha=1}^N \frac{\hbar \tilde{\omega}_{\alpha}}{2} (\tilde{p}_{\alpha}^2 + \bar{q}_{\alpha}^2) - \hbar \omega_0 \sum_{\alpha=1}^N \tilde{\kappa}_{\alpha} \bar{q}_{\alpha} q_0, \quad (\text{B12})$$

where

$$\bar{\lambda}_x = \lambda_x - \sum_{\alpha=1}^N \frac{\tilde{\omega}_{\alpha}}{2} \kappa_{\alpha}^2 \left(\frac{\omega_0}{\tilde{\omega}_{\alpha}} \right)^2 (d_x^{(0)})^2 \quad (\text{B13})$$

and

$$\bar{d}_x = \left(1 - \sum_{\alpha=1}^N \tilde{\kappa}_{\alpha}^2 \frac{\omega_0}{\tilde{\omega}_{\alpha}} \right) d_x^{(0)}. \quad (\text{B14})$$

From the Hamiltonian in Eq. (B12), it becomes clear that one can define $N+1$ new normal modes that include all \bar{q}_{α} and q_0 so that the last term is eliminated. Written in such normal

modes $q'_a = \sum_{\alpha} c_{\alpha}^{(a)} \bar{q}_{\alpha}$ ($\bar{q}_{\alpha} = \sum_{\alpha} c_{\alpha}^{(\alpha)} q'_a$), the Hamiltonian reads as

$$H_x = \sum_{a=0}^N \frac{\hbar \omega'_a}{2} (p_a'^2 + q_a'^2) + \hbar \bar{\lambda}_x - \sum_{a=0}^N \hbar \omega'_a d_x^{(a)} q'_a, \quad (\text{B15})$$

where $d_x^{(a)} = (\omega_0/\omega'_a) \bar{d}_x c_a^{(0)}$. Equation (B15) has the form of Eq. (B5), and thus, the effective Brownian coordinate model can always be represented by a multimode bath.

3. Bath correlation function: Continuous spectral density

The system-bath interaction driven by the Hamiltonian of Eq. (B7) at a given electronic state $|x\rangle$ is characterized by the correlation function

$$\begin{aligned} C^{(xx)}(t) &= \frac{1}{\hbar^2} \langle \Delta W_{xg}(t) \Delta W_{xg}(0) \rangle_{\text{eq}} \\ &= \sum_k \omega_k^2 (d_x^{(k)})^2 \langle q_k(t) q_k(0) \rangle_{\text{eq}}, \end{aligned} \quad (\text{B16})$$

where $\langle \cdots \rangle_{\text{eq}}$ represents the averaging (trace) over the equilibrium state of the bath. Introducing the density of states $\rho(\omega)$,

$$\rho(\omega) = \sum_k \delta(\omega - \omega_k), \quad (\text{B17})$$

which gives the number of vibrational modes with frequency in the interval (ω_1, ω_2) as $\int_{\omega_1}^{\omega_2} \rho(\omega) d\omega$, and the spectral density

$$J^{(x)}(\omega) = \rho(\omega) (d_x(\omega))^2 = \sum_k (d_x^{(k)})^2 \delta(\omega - \omega_k), \quad (\text{B18})$$

we can write

$$C^{(xx)}(t) = \int_0^\infty d\omega \omega^2 J^{(x)}(\omega) \langle q_\omega(t) q_\omega(0) \rangle_{\text{eq}}. \quad (\text{B19})$$

For simplicity, we have stopped writing out the limits of the summations explicitly. The spectral density defined in Eq. (B18) is a standard quantity used to describe the bath in theories of open quantum systems.¹¹ If the distribution of the modes in $\rho(\omega)$ is very dense, we may work with $J^{(x)}(\omega)$ as if it was a continuous function. The bath is therefore represented by a large continuous set of noninteracting vibrational modes that are in equilibrium. The coordinate correlation function of a mode with frequency ω can be calculated directly via

$$\begin{aligned} \langle q_\omega(t) q_\omega(0) \rangle_{\text{eq}} &= \text{tr} \{ U^\dagger(t) q U(t) q W_{\text{eq}} \} \\ &= e^{-i\omega t} [n(\omega, T) + 1] + e^{i\omega t} n(\omega, T), \end{aligned} \quad (\text{B20})$$

where we denote the Bose–Einstein distribution as

$$n(\omega, T) = \frac{1}{e^{\hbar\omega/k_B T} - 1}. \quad (\text{B21})$$

Thus, the correlation function $C^{(xx)}(t)$ has the form of a Fourier transform of the following function:

$$\begin{aligned} C^{(xx)}(\omega) &= 2\pi\omega^2 [1 + n(\omega, T)] \\ &\times [\theta(\omega) J^{(x)}(\omega) - \theta(-\omega) J^{(x)}(-\omega)]. \end{aligned} \quad (\text{B22})$$

The generalization of the model on a cross-correlation function $C^{(xy)}(t)$ is rather straightforward. Analogous to Eq. (B16), we write

$$\begin{aligned} C^{(xy)}(t) &= \sum_k \omega_k^2 d_x^{(k)} d_y^{(k)} \langle q_k(t) q_k(0) \rangle_{\text{eq}} \\ &= \int_0^\infty d\omega \omega^2 J^{(xy)}(\omega) \langle q_k(t) q_k(0) \rangle_{\text{eq}}. \end{aligned} \quad (\text{B23})$$

The new spectral density $J^{(xy)}(t)$ reflects the overlap of the distribution of displacements $d_x^{(k)}$ and $d_y^{(k)}$ over the bath modes. Assuming a continuous distribution of the modes, we can introduce a displacement distribution $D(\omega)$ as

$$\begin{aligned} D(\omega) &= \sum_k d^{(k)} \delta(\omega - \omega_k) \rightarrow \int d\omega' d(\omega') \delta(\omega - \omega') \\ &= d(\omega). \end{aligned} \quad (\text{B24})$$

We are interested in the spectral density

$$\begin{aligned} J^{(xy)}(\omega) &= \sum_k d_x^{(k)} d_y^{(k)} \delta(\omega - \omega_k) \\ &= \sum_{kl} d_x^{(k)} d_y^{(l)} \delta(\omega - \omega_k) \delta_{kl} \\ &\rightarrow \int_{-\infty}^\infty d\omega' \int_{-\infty}^\infty d\omega'' d_x(\omega') d_y(\omega'') \delta(\omega - \omega') \\ &\times \delta(\omega' - \omega''). \end{aligned} \quad (\text{B25})$$

Thus, we can write

$$J^{(xy)}(\omega) = d_x(\omega) d_y(\omega) = D^{(x)}(\omega) D^{(y)}(\omega), \quad (\text{B26})$$

and consequently, also

$$J^{(xx)}(\omega) = (D^{(x)}(\omega))^2. \quad (\text{B27})$$

The cross-correlation function is obtained from an overlap of the respective displacement distributions of the two electronic states. Unlike the spectral density, the displacement distribution is not necessarily positive for all values of ω .

4. Bath correlation function: Multiple spectral densities

The continuous model of the spectral density as discussed above assumes continuous oscillator displacements $D^{(e)}(\omega) \equiv d_e(\omega)$ and $D^{(f)}(\omega) \equiv d_f(\omega)$. This model is not able to describe a general situation of several independent effective Brownian coordinates. Let us assume just two effective Brownian modes interacting with two transitions $|g\rangle \rightarrow |e\rangle$ and $|g\rangle \rightarrow |f\rangle$. We cannot assign a single distribution of the displacements, say $D^{(e)}(\omega) = D_1^{(e)}(\omega) + D_2^{(e)}(\omega)$, to the electronic levels. This can be seen simply from the fact that the expected total correlation function $C^{(ee)}(t)$ is a sum of the correlation functions $C^{(ee)}(t) = C_1^{(ee)}(t) + C_2^{(ee)}(t)$ from which it follows that $J^{(ee)}(\omega) = (D_1^{(e)}(\omega))^2 + (D_2^{(e)}(\omega))^2 \neq (D^{(e)}(\omega))^2$. Clearly, $D_n^{(e)}(\omega)$ behave as components of a vector

$$\mathbf{D}^{(e)}(\omega) = \xi_1 \mathbf{D}_1^{(e)}(\omega) + \dots + \xi_N \mathbf{D}_N^{(e)}(\omega) \quad (\text{B28})$$

and $J^{(ee)}(\omega)$ is the scalar product of such a vector

$$J^{(ee)}(\omega) = \mathbf{D}^{(e)}(\omega) \cdot \mathbf{D}^{(e)}(\omega). \quad (\text{B29})$$

Correspondingly,

$$J^{(ef)}(\omega) = \mathbf{D}^{(e)}(\omega) \cdot \mathbf{D}^{(f)}(\omega). \quad (\text{B30})$$

A given transition can be assigned a single spectral density $J(\omega)$, but in general, it cannot be assigned a single displacement distribution. A pair of transitions can also be assigned a spectral density, but it is not possible to construct it based on the spectral densities of the individual transitions. Rather, the cross spectral density is obtained from the vectors of the displacement distributions as in Eq. (B30). For a general multicomponent bath, there is an upper limit for the absolute value of the cross spectral density

$$|J^{(ef)}(\omega)| \leq |\mathbf{D}^{(e)}(\omega)| |\mathbf{D}^{(f)}(\omega)|, \quad (\text{B31})$$

but no lower bound other than the obvious $|J^{(ef)}(\omega)| \geq 0$ can be identified.

¹F. Milota, J. Sperling, A. Nemeth, T. Mančal, and H. F. Kauffmann, *Acc. Chem. Res.* **42**, 1364 (2009).

²T. Joo, Y. Jia, J.-Y. Yu, M. J. Lang, and G. R. Fleming, *J. Chem. Phys.* **104**, 6089 (1996).

³W. P. de Boeij, M. S. Pshenichnikov, and D. A. Wiersma, *Annu. Rev. Phys. Chem.* **49**, 99 (1998).

⁴M. H. Cho, *Chem. Rev. (Washington, D.C.)* **108**, 1331 (2008).

⁵D. M. Jonas, *Annu. Rev. Phys. Chem.* **54**, 425 (2003).

⁶S. Mukamel, *Principles of Nonlinear Optical Spectroscopy* (Oxford University Press, Oxford, 1995).

⁷M. Khalil, N. Demirdöven, and A. Tokmakoff, *Phys. Rev. Lett.* **90**, 047401 (2003).

⁸S. Mukamel, R. Oszwaldowski, and L. Yang, *J. Chem. Phys.* **127**, 221105 (2007).

⁹D. Abramavicius, D. V. Voronine, and S. Mukamel, *Proc. Natl. Acad. Sci. U.S.A.* **105**, 8525 (2008).

¹⁰E. C. Fulmer, P. Mukherjee, A. T. Krummel, and M. T. Zanni, *J. Chem. Phys.* **120**, 8067 (2004).

¹¹V. May and O. Kühn, *Charge and Energy Transfer Dynamics in Molecular Systems* (Wiley-VCH, Berlin, 2000).

¹²L. Yang and S. Mukamel, *Phys. Rev. Lett.* **100**, 057402 (2008).

¹³Z. Y. Li, D. Abramavicius, and S. Mukamel, *J. Am. Chem. Soc.* **130**, 3509 (2008).

¹⁴K. W. Stone, D. Turner, K. Gundogdu, S. T. Cundiff, and K. A. Nelson, *Acc. Chem. Res.* **42**, 1452 (2009).

¹⁵K. W. Stone, K. Gundogdu, D. Turner, X. Li, S. T. Cundiff, and K. A. Nelson, *Science* **324**, 1169 (2009).

¹⁶J. Kim, V. M. Huxter, C. Curutchet, and G. D. Scholes, *J. Phys. Chem. A* **113**, 12122 (2009).

¹⁷J. Kim, S. Mukamel, and G. D. Scholes, *Acc. Chem. Res.* **42**, 1375 (2009).

¹⁸L. J. Yang, T. H. Zhang, A. D. Bristow, S. T. Cundiff, and S. Mukamel, *J. Chem. Phys.* **129**, 234711 (2008).

¹⁹D. Karaickaj, A. D. Bristow, L. Yang, X. Dai, R. P. Mirin, S. Mukamel, and S. T. Cundiff, *Phys. Rev. Lett.* **104**, 117401 (2010).

²⁰K. Schulten, I. Ohmine, and M. Karplus, *J. Chem. Phys.* **64**, 4422 (1976).

²¹R. W. Chambers and D. R. Kearns, *Photochem. Photobiol.* **10**, 215 (1969).

²²M. Chachisvilis, O. Kuhn, T. Pullerits, and V. Sundström, *J. Phys. Chem. B* **101**, 7275 (1997).

²³D. Zigmantas, E. L. Read, T. Mančal, T. Brixner, A. T. Gardiner, R. J.

Cogdell, and G. R. Fleming, *Proc. Natl. Acad. Sci. U.S.A.* **103**, 12672 (2006).

²⁴M. Becker, V. Nagarajan, and W. W. Parson, *J. Am. Chem. Soc.* **113**, 6840 (1991).

²⁵P. Malý, R. Danielius, and R. Gadonas, *Photochem. Photobiol.* **45**, 7 (1987).

²⁶B. Brüggemann, N. Christensson, and T. Pullerits, *Chem. Phys.* **357**, 140 (2009).

²⁷F. Milota, J. Sperling, A. Nemeth, and H. F. Kauffmann, *Chem. Phys.* **357**, 45 (2009).

²⁸E. Riedle, M. Beutter, S. Lochbrunner, J. Piel, S. Schenkl, S. Spörlein, and W. Zinth, *Appl. Phys. B: Lasers Opt.* **71**, 457 (2000).

²⁹P. Baum, M. Breuer, E. Riedle, and G. Steinmeyer, *Opt. Lett.* **31**, 2220 (2006).

³⁰A. Nemeth, J. Sperling, J. Hauer, H. F. Kauffmann, and F. Milota, *Opt. Lett.* **34**, 3301 (2009).

³¹K. Gundogdu, K. W. Stone, D. B. Turner, and K. A. Nelson, *Chem. Phys.* **341**, 89 (2007).

³²T. Brixner, I. V. Stiopkin, and G. R. Fleming, *Opt. Lett.* **29**, 884 (2004).

³³J. D. Hybl, A. A. Ferro, and D. M. Jonas, *J. Chem. Phys.* **115**, 6606 (2001).

³⁴S. M. Gallagher, A. W. Albrecht, J. D. Hybl, B. L. Landin, B. Rajaram, and D. M. Jonas, *J. Opt. Soc. Am. B* **15**, 2338 (1998).

³⁵T. Brixner, T. Mančal, I. V. Stiopkin, and G. R. Fleming, *J. Chem. Phys.* **121**, 4221 (2004).

³⁶A. D. Bristow, D. Karaickaj, X. Dai, and S. T. Cundiff, *Opt. Express* **16**, 18017 (2008).

³⁷E. H. G. Backus, S. Garrett-Roe, and P. Hamm, *Opt. Lett.* **33**, 2665 (2008).

³⁸A. Moran, S. Park, and N. Scherer, *J. Phys. Chem. B* **110**, 19771 (2006).

³⁹M. J. Tauber, R. A. Mathies, X. Chen, and S. E. Bradforth, *Rev. Sci. Instrum.* **74**, 4958 (2003).

⁴⁰S. Laimgruber, H. Schachenmayr, B. Schmidt, W. Zinth, and P. Gilch, *Appl. Phys. B: Lasers Opt.* **85**, 557 (2006).

⁴¹S. T. Roberts, J. J. Loparo, and A. Tokmakoff, *J. Chem. Phys.* **125**, 084502 (2006).

⁴²K. Lazonder, M. S. Pshenichnikov, and D. A. Wiersma, *Opt. Lett.* **31**, 3354 (2006).

⁴³J. D. Hybl, Y. Christophe, and D. M. Jonas, *Chem. Phys.* **266**, 295 (2001).

⁴⁴N. Christensson, F. Milota, A. Nemeth, J. Sperling, H. F. Kauffmann, T. Pullerits, and J. Hauer, *J. Phys. Chem. B* **113**, 16409 (2009).

⁴⁵E. C. Fulmer, F. Ding, and M. T. Zanni, *J. Chem. Phys.* **122**, 034302 (2005).

⁴⁶S. Mukamel and D. Abramavicius, *Chem. Rev. (Washington, D.C.)* **104**, 2073 (2004).

⁴⁷J. Sung and R. J. Silbey, *J. Chem. Phys.* **115**, 9266 (2001).

⁴⁸S. Shim, C. M. Stuart, and R. A. Mathies, *ChemPhysChem* **9**, 697 (2008).

⁴⁹N. Christensson, T. Polivka, A. Yartsev, and T. Pullerits, *Phys. Rev. B* **79**, 245118 (2009).

⁵⁰P. R. Hammond, *IEEE J. Quantum Electron.* **16**, 1157 (1980).

⁵¹E. R. Smith, D. A. Farrow, and D. M. Jonas, *J. Chem. Phys.* **123**, 12 (2005).

⁵²K. Raghavachari and J. B. Anderson, *J. Phys. Chem.* **100**, 12960 (1996).

⁵³E. Papagiannakis, I. H. M. van Stokkum, M. Vengris, R. J. Cogdell, R. van Grondelle, and D. S. Larsen, *J. Phys. Chem. B* **110**, 527 (2006).

⁵⁴J. Savolainen, T. Buckup, J. Hauer, A. Jafarpour, C. Serrat, M. Motzkus, and J. L. Herek, *Chem. Phys.* **357**, 181 (2009).

⁵⁵P. Hamm, M. Lim, and R. M. Hochstrasser, *Phys. Rev. Lett.* **81**, 5326 (1998).

⁵⁶E. W. Knapp, *Chem. Phys.* **85**, 73 (1984).

⁵⁷J. P. Lemaistre, *Chem. Phys.* **246**, 283 (1999).

⁵⁸A. Nemeth, V. Lukeš, J. Sperling, F. Milota, H. F. Kauffmann, and T. Mančal, *Phys. Chem. Chem. Phys.* **11**, 5986 (2009).

⁵⁹F. Milota, J. Sperling, A. Nemeth, D. Abramavicius, S. Mukamel, and H. F. Kauffmann, *J. Chem. Phys.* **131**, 054510 (2009).

⁶⁰G. M. Alber and A. G. Marshall, *Appl. Spectrosc.* **44**, 1111 (1990).